Dynamics of Landfalling Atmospheric Rivers over the North Pacific in 30 Years of MERRA Reanalysis

ASHLEY E. PAYNE AND GUDRUN MAGNUSDOTTIR

Department of Earth System Science, University of California, Irvine, Irvine, California

(Manuscript received 2 January 2014, in final form 22 June 2014)

ABSTRACT

A large-scale analysis of landfalling atmospheric rivers (ARs) along the west coast of North America and their association with the upper-tropospheric flow is performed for the extended winter (November–March) for the years 1979–2011 using Modern-Era Retrospective Analysis for Research and Applications (MERRA) reanalysis data. The climatology, relationship to the El Niño–Southern Oscillation and the Madden–Julian oscillation, and upper-level characteristics of approximately 750 landfalling ARs are presented based on the 85th percentile of peak daily moisture flux. AR occurrence along the West Coast is dominated by early season events. In composites of upper-level fields during AR occurrences, certain characteristics stand out irrespective of the tropical climate indices. This suggests that extratropical dynamical processes play a key role in AR dynamics.

The influence of the large-scale circulation on AR intensity prior to landfall is examined by objectively selecting an extreme subset of 112 landfalling AR dates representing the 95th percentile of strongest cases. Each landfalling AR date that is identified is traced backward in time using a novel semiautomated tracking algorithm based on spatially and temporally connected organized features in integrated moisture transport. Composites of dynamical fields following the eastward progression of ARs show a close relationship of the location of the jet, Rossby wave propagation, and anticyclonic Rossby wave breaking in the upper troposphere of the eastern Pacific and moisture transport in the lower troposphere. Comparison between the strongest and the weakest ARs within the most extreme subset shows differences in both the intensity of moisture transport and the scale and development of anticyclonic Rossby wave breaking in the eastern Pacific.

1. Introduction

Atmospheric rivers (ARs) are filamentary features with high water vapor content in the lower troposphere that are important for the poleward transport of atmospheric moisture globally (Zhu and Newell 1998). They develop on synoptic time scales, generally in association with low-level moisture convergence within extratropical cyclones, and appear as spatially narrow plumes of moisture that can stretch over thousands of kilometers in the lower troposphere. While ARs form in association with the warm conveyor belt of extratropical cyclones, they are not necessarily uniquely associated with a single cyclone, and an AR can span the lifetimes of multiple cyclones (Newman et al. 2012; Sodemann and Stohl 2013).

AR formation in the northern Pacific basin is of particular interest due to their well-documented effects on land. Along the western coastline of North America, ARs have been connected to heavy precipitation, flooding, and snowpack variability when they cross over land (so-called landfall) (Ralph et al. 2006; Neiman et al. 2008a; Smith et al. 2010; Dettinger et al. 2011; Guan et al. 2012). Their landfall is important to water resources, particularly within the contiguous United States where they have been shown to contribute between 30% and 50% of wet season precipitation (Guan et al. 2010; Dettinger et al. 2011). Up to three-quarters of persistent droughts along the West Coast have been ended by a landfalling AR storm (Dettinger 2013). Although they operate on rather short time scales, depending on their intensity and synoptic characteristics upon landfall, a relatively small number of these storms can be the difference between dry and wet years (Dettinger et al. 2011; Dettinger 2013).

Despite well-documented hydrological impacts and meteorological characteristics of landfalling ARs, the large-scale flow influencing ARs prior to landfall is still

Corresponding author address: Ashley E. Payne, Department of Earth System Science, University of California, Irvine, 3200 Croul Hall, Irvine, CA 92697.
E-mail: aepayne@uci.edu

DOI: 10.1175/JCLI-D-14-00034.1

an area of active research and has received much attention recently (Ralph et al. 2011; Guan et al. 2010, 2012, 2013; Lavers et al. 2012). In animations and in snapshots of moisture transport over the world's ocean basins, as seen in the reanalysis data that we use, the nearly constant presence of ARs in both hemispheres is striking and this was commented on in early studies (e.g., Newell et al. 1992; Zhu and Newell 1998). Those ARs that intersect the West Coast and make landfall vary in moisture source region, trajectory, and intensity (Neiman et al. 2008b). Knowledge of modulating factors is needed to address current challenges in AR forecasting and projections of their distribution, intensity, and frequency with future climate change.

Work over the Pacific basin has focused on the roles of El Niño–Southern Oscillation (ENSO), the Madden–Julian oscillation (MJO), and the Pacific–North American pattern (PNA) in modulating ARs (Higgins et al. 2000; Bao et al. 2006; Ryoo et al. 2013; Mo and Higgins 1998a,b; Jones 2000; Ralph et al. 2011; Guan et al. 2012, 2013). Most of these studies have based their conclusions on correlations between the signatures of ARs on land (such as total rainfall and snow water equivalent) and climate mode indices, rather than direct detection of ARs and the dynamical processes driving them. Very few studies have focused on the evolution of the feature itself over the Pacific prior to landfall. Ralph et al. (2011) performed a detailed case study of the development of a single AR over the Pacific basin and attempted to tie its formation and behavior to changes in moisture availability due to the progression of the MJO in the tropics. In the context of the impacts of ENSO on the background flow, Ryoo et al. (2013) found that moisture transport is modulated by both the strength of the subtropical jet and the location of Rossby wave breaking along the west coast of North America. Both of these studies suggest a role for large-scale dynamics in modulating ARs prior to landfall.

The scope of the research on large-scale influences on ARs is limited both by the ability of each study to sample ARs and by the complexity of the multiscale processes contributing toward AR behavior prior to landfall. Because of these limitations, it is difficult to make sweeping conclusions as to the dominant mechanisms contributing to variations in AR behavior prior to landfall. Understanding how large-scale dynamical factors influence ARs over the Pacific in the observational record is essential to our understanding of the role ARs will play in the hydrological cycle in a warmer climate.

Here we examine the climatological characteristics of landfalling ARs on the West Coast, defined by the 85th percentile of peak daily moisture transport (Lavers et al. 2012), over the extended winter period from 1979 to 2011. To examine their behavior prior to landfall, we develop a backtracking algorithm based on moisture flux to resolve the progression of ARs across the basin in composites. We detail the dynamical influences on the behavior of an extreme subset of ARs that have been tracked over the Pacific basin in a reanalysis product covering more than 30 years of data. We address the following questions: 1) what is the relationship between ARs and upper-level dynamics and 2) what influences the intensity of ARs prior to landfall?

This paper is organized as follows. Data and methodology for identifying landfalling ARs, as well as selecting the cases that make up our backtracked extreme subset, are described in sections 2 and 3. In section 4, we provide an overview of the characteristics of landfalling ARs over the extended winter for the years 1979–2011. Section 4 also shows the relationship between moisture flux over the basin and upper-level dynamics using the extreme subset of ARs. In section 5, we show the connection of AR intensity to Rossby wave propagation and breaking. At the end of section 5, we put our results linking ARs to Rossby wave breaking in context by showing the difference between breaking frequency and extent for landfalling AR dates compared to the climatology for the entire extended winter. The conclusions of this study and their implications are found in section 6.

2. Data

We use the Modern-Era Retrospective Analysis for Research and Applications (MERRA) reanalysis dataset, available starting from 1979 from the National Aeronautics and Space Administration (NASA). Use of the MERRA product has significant advantages as it is of high spatial and temporal resolution and was developed specifically for application to the hydrological cycle (Rienecker et al. 2011). Specific humidity, horizontal winds, and potential vorticity were retrieved from pressure levels at reduced spatial resolution (1.25° × 1.25°) at 3-hourly intervals. Total surface precipitation was retrieved at native spatial resolution (⅔° × ½°) at 1-hourly intervals. (Precipitation data are converted from units of kg m^{-2} s^{-1} to units of mm and then averaged every three time steps.) The precipitation data at 3-hourly intervals are linearly interpolated to reduced spatial resolution for use with the moisture and dynamical fields.

The behavior of the ARs is examined with respect to both the MJO and ENSO using the daily real-time multivariate MJO (RMM) index and the monthly multivariate ENSO index (MEI), respectively (Wheeler and Hendon 2004; Wolter and Timlin 1998). MJO activity with a RMM amplitude below 1 is considered too weak to have large-scale impacts on circulation and is not

considered in the following analysis. El Niño events are indicated by MEI values greater than 0.5 and La Niña events are indicated by MEI values less than −0.5. For each landfalling AR date, the MJO phase (provided the amplitude is greater than 1) and the prevailing state of ENSO are recorded.

3. Methods

a. AR visualization

As has been pointed out by previous researchers (e.g., Bao et al. 2006; Newman et al. 2012), ARs do not represent trajectories of moisture as their name might suggest, but are rather constantly evolving pathways for moisture transport, recycling moisture between the atmosphere and the underlying ocean as they move over basins. Observational researchers have long used vertically integrated water vapor content—also known as total precipitable water, measured in centimeters of liquid water equivalent—as a proxy for water vapor transport accomplished in ARs (Ralph et al. 2004, 2005; Neiman et al. 2008b; Jiang and Deng 2011; Wick et al. 2013a,b). However, the use of integrated moisture is primarily motivated by a lack of in situ low-level wind data over oceanic regions. The use of a dynamically consistent reanalysis dataset makes direct investigation of moisture transport possible.

We follow the methodology in Lavers et al. (2012) to simplify our analysis and define the magnitude of the vertically integrated moisture flux (MF), as follows:

$$\mathrm{MF}(\lambda,\phi,t) = g^{-1}\int_{p_s}^{p_t} q(\lambda,\phi,p,t)|\mathbf{v}(\lambda,\phi,p,t)|\,dp, \qquad (1)$$

where $|\mathbf{v}|$ is the horizontal wind speed on isobaric surfaces (measured in units of $\mathrm{m\,s^{-1}}$), q is specific humidity (measured in units of $\mathrm{kg\,kg^{-1}}$), g is the gravitational acceleration ($9.81\,\mathrm{m\,s^{-2}}$), p_s is 1000 hPa, and p_t is 700 hPa. Over the Pacific basin the influence of the jet stream dominates above 700 hPa, whereas water vapor drops off very quickly with height. While previous researchers have integrated to 300 hPa, we found that vertical integration to 700 hPa was appropriate.

b. AR dataset construction

Our focus is on wintertime ARs (November–March), as they have been shown to have higher moisture transport and have greater impacts on land (Neiman et al. 2008b). It is important to note that we exclude the month of October in our selection of landfalling dates. Several significant ARs have made landfall during October, impacting the Pacific Northwest in particular, generally related to recurving transitional tropical cyclones (Lynott and Cramer 1966; Ralph et al. 2011). However, because October is a transition season that has many characteristics of late summer, it is very difficult to detect organized structures in MF over the Pacific basin. The ARs making landfall during October have largely different characteristics in both trajectory and in moisture transport from the ARs making landfall in November–March.

For each date between 1 November and 31 March for the years 1979–2011, we record two values: peak daily MF and total daily precipitation. These two values are calculated as follows. For each date, daily mean MF and precipitation are isolated over a seven-gridpoint region centered on the western coastline of North America between 20° and 60°N (Figs. 1a,b). Within the outlined region in Fig. 1a, each variable is averaged in the zonal direction. The blue and orange lines in Fig. 1c show the seven-point averaged distributions for MF and precipitation, respectively. For each date, the peak MF and the total precipitation, summed over a 17-gridpoint window in the latitudinal direction and centered on the peak MF, are recorded (Fig. 1c). Figure 1c shows an example of the 17-point range over which precipitation is summed and the values recorded for peak MF and total precipitation for 3 December 2007. The two values recorded for each date over the entire time period are illustrated in Fig. 2, which shows the distribution of all dates, sorted according to the peak daily MF (black line) and plotted with each date's total precipitation (light gray line).

We use two landfalling AR datasets in our study: 1) a climatology of all landfalling AR dates to impact the western coast of North America between 20° and 60°N between the years 1979 and 2011 and 2) a backtracked subset of the climatology, isolating only the most extreme AR events to make landfall. The details of our methodology follow, where section 3b(1) describes how we define our landfalling AR climatology, section 3b(2) describes how we isolate an extreme subset of landfalling AR dates from our climatology, and section 3b(3) details our backtracking methods for the extreme subset of landfalling ARs.

1) Climatology

We define a climatology of landfalling AR dates using the 85th percentile on peak daily MF [generally following the methods in Lavers et al. (2012)], where landfall is defined by physical proximity to the coastline of North America. Landfalling AR dates are all those dates in the time period with peak daily MF values greater than or equal to the 85th percentile ($233\,\mathrm{kg\,m^{-1}\,s^{-1}}$). The vertical dark gray line in Fig. 2 shows the 85th percentile of peak daily MF, where all dates to the right are labeled as landfalling AR dates. The green dots in Fig. 2 show the locations of nine notable landfalling AR events, as listed

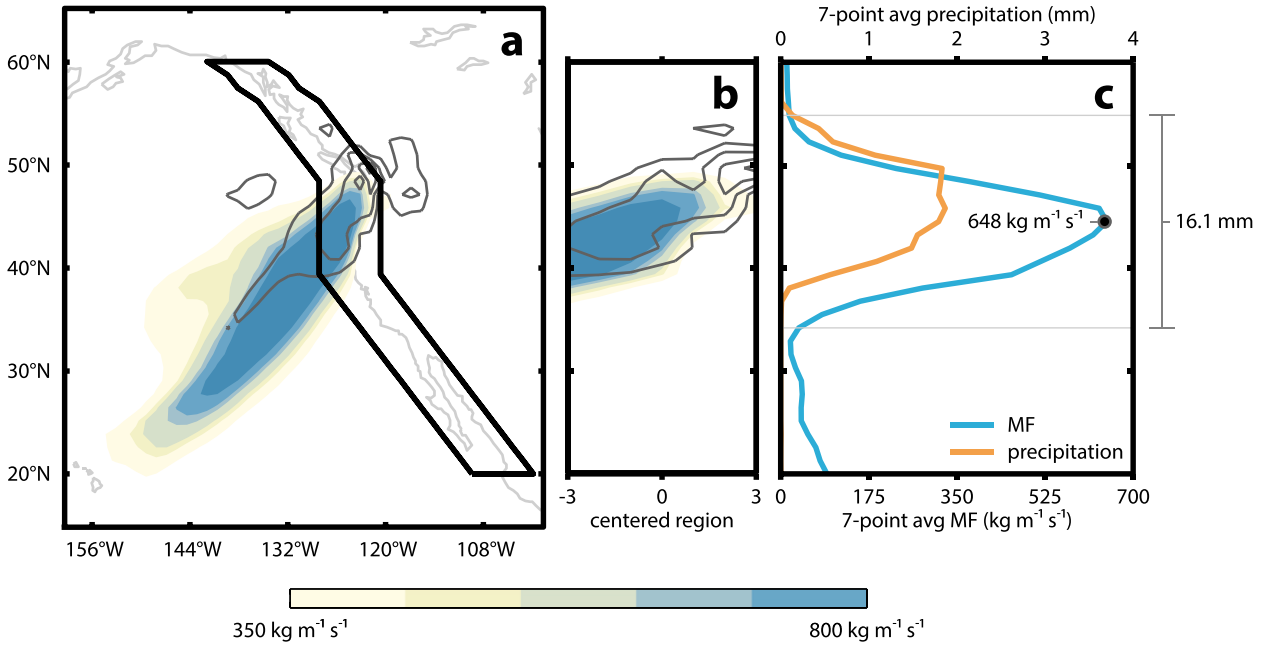

FIG. 1. Example of the case selection methodology applied to 3 Dec 2007. (a) For each day in the time period considered, daily mean MF ($kg\,m^{-1}\,s^{-1}$, shaded) and daily mean precipitation (mm, contoured starting at 0.5 mm and increasing in intervals of 1 mm) are isolated in the region outlined in black, where (b) shows a straightened image of the two variables within the region. (c) The two variables are then averaged over 7 grid points in the zonal direction. For each day, two values are recorded: the peak in daily mean 7-point averaged MF (blue line) and the sum of daily mean 7-point averaged precipitation over a 17-point range in the latitudinal direction, centered on the peak MF. As an example, for 3 Dec 2007, the boundaries of the 17-point range are shown in the horizontal gray lines in (c) and where the two values recorded are $648\,kg\,m^{-1}\,s^{-1}$ (peak daily MF) and 16.1 mm (total daily precipitation).

on the National Oceanic and Atmospheric Administration (NOAA)/Earth System Research Laboratory AR information page (http://www.esrl.noaa.gov/psd/atmrivers/events/).

2) SUBSET OF EXTREME CASES—SELECTION

As we are unable to distinguish multiday landfalling events or examine ARs prior to landfall with the climatology of landfalling ARs just described, case selection becomes necessary for in-depth analysis. We objectively isolate a subset of landfalling AR days that can then be extended backward in time using our tracking algorithm. We emphasize that no part of our case selection procedure is subjective. While our focus is on the intensity of ARs preceding landfall, rather than on any orographic influences, we recognize the importance of characterizing ARs as extreme precipitation events. Therefore, both peak daily MF and total daily precipitation are used to select landfalling dates for our extreme subset.

Two thresholds are used to reduce the sample size for the purposes of a more detailed study and to retain the most extreme events to impact the coast. The 95th percentiles for all dates in the time period are calculated for the peak daily MF and associated total daily precipitation (MF threshold: $305\,kg\,m^{-1}\,s^{-1}$, precipitation threshold: 8.24 mm). All dates with peak daily MF and total daily precipitation that fall below the thresholds are discarded. The two thresholds for peak daily MF and total daily precipitation are shown as blue and orange lines, respectively, in Fig. 2.

A criterion is put in place to eliminate the possibility that the subset is dominated by a few large, slow moving events off the coast. For all dates with values greater than the two thresholds, they must be separated by at least three days. This means that, if two days with fewer than three days separation have sufficiently high values of peak daily MF and total daily precipitation, the date with the greater peak daily MF is retained and the date with the lower peak daily MF is discarded. Applying this logic, of all dates that had values above the set thresholds (127 dates total), 15 were discarded. Of the 15 dates discarded, 11 dates were part of the same multiday landfalling AR event as a previously selected date. The four remaining dates (7 January 1990, 2 February 1991, 10 December 1995, and 16 December 2002) belong to landfalling AR events directly preceding or directly following previously selected dates.

Of the nine notable landfalling AR events mentioned previously (green dots in Fig. 2), only four events satisfy our criteria on both peak daily MF and total daily

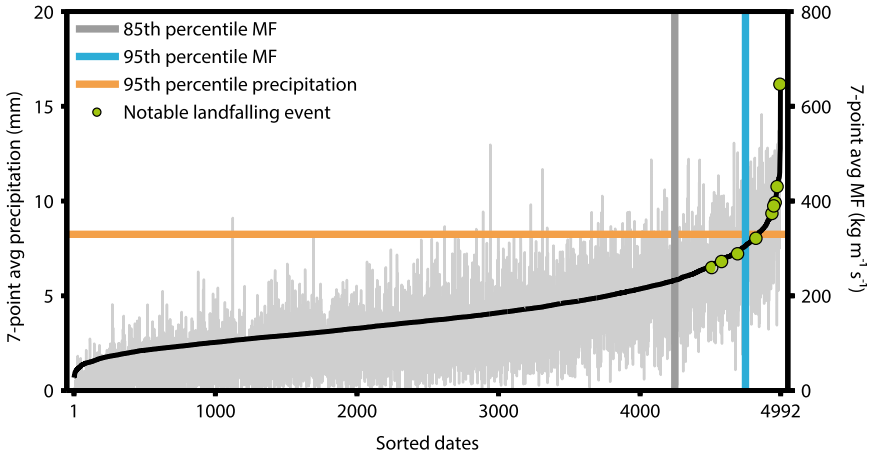

FIG. 2. The distribution of all dates in our time period [November–March (NDJFM), 1979–2011] sorted according to the peak daily MF ($kg\,m^{-1}\,s^{-1}$, black line) and plotted with the associated total daily precipitation (mm, light gray line). The dark gray line shows the 85th percentile and dates to the right of this line are labeled as landfalling AR dates (749 total). Our extreme subset of cases are selected from all landfalling AR dates, with values above both the 95th percentile of peak daily MF (blue line) and the 95th percentile of total daily precipitation (orange line), with at least three days of separation. For validation of this methodology, nine significant landfalling events (11–24 Feb 1986, 29 Dec 1996–4 Jan 1997, 2–3 Feb 1998, 16–18 Feb 2004, 7–11 Jan 2005, 25–27 Mar 2005, 29 Dec 2005–2 Jan 2006, 6–7 Nov 2006, and 6–8 Jan 2009) are indicated by green points (multiday events use the date with the highest peak daily MF).

precipitation: 11–24 February 1986, 29 December 1996–4 January 1997, 29 December 2005–2 January 2006, and 6–7 November 2006. These four events produced some of the largest flooding in the Pacific Northwest over the last 50 years and confirm that our case selection process does indeed isolate the most extreme landfalling ARs. When the month of October is considered, the dates originally selected remain largely the same, with 106 of the selected dates remaining the same and 19 dates being added due to October events. With improvements to our tracking methodology (description to follow) we may be able to investigate these transitional season landfalling ARs in the future.

3) TRACKING

We developed a semiautomated algorithm to track the centroid of each selected AR back in time, over the course of its lifetime. Most previous studies only consider the few days right around AR landfall. Here, our aim is to study the development of the events, expanding the timeline of a single event beyond the few days of its landfall.

ARs are visualized over the basin, prior to landfall, using MF imagery with a static threshold of $350\,kg\,m^{-1}\,s^{-1}$. This threshold is only meant to separate peaks in MF from background moisture prior to landfall, over the basin, and is not used in any way to define the two datasets previously described. Moderately increasing or decreasing this threshold only changed slightly the number of grid points attributed to an AR and the location of its centroid, but ultimately did not affect the detection of the feature itself as an intense flux of moisture. For each time step, connected grid points forming a unified area poleward of 23.5°N (focus on the extratropics) and greater than an area threshold of $21\,000\,km^2$ were labeled as an instantaneous snapshot of a single AR (Fig. 3, top panel). The area threshold is chosen to retain only the larger-scale features. Characteristics such as the location of the centroid (the center of mass of the feature) and orientation (the angle between a line of latitude and the major axis of the feature) of the AR were recorded at each time step. It should be noted that this algorithm cannot detect the exact moment of formation of the AR. However, because the focus of our study is to investigate the factors contributing to AR intensity rather than its formation, we consider the identification of its first appearance as an organized feature in the extratropics to be a good approximation.

We define the lifetime of an AR to be the series of instantaneous snapshots of connected grid points that are linked through time. An example of our process is shown in Fig. 3. Through the process described above, we identify the centroids of each possible AR over the Pacific basin at each time step. The time-intensive part of our method comes with the manual recording of the selected AR's centroid over each time step. While an automated method to track connected features in both space and time was developed, it was discarded pending

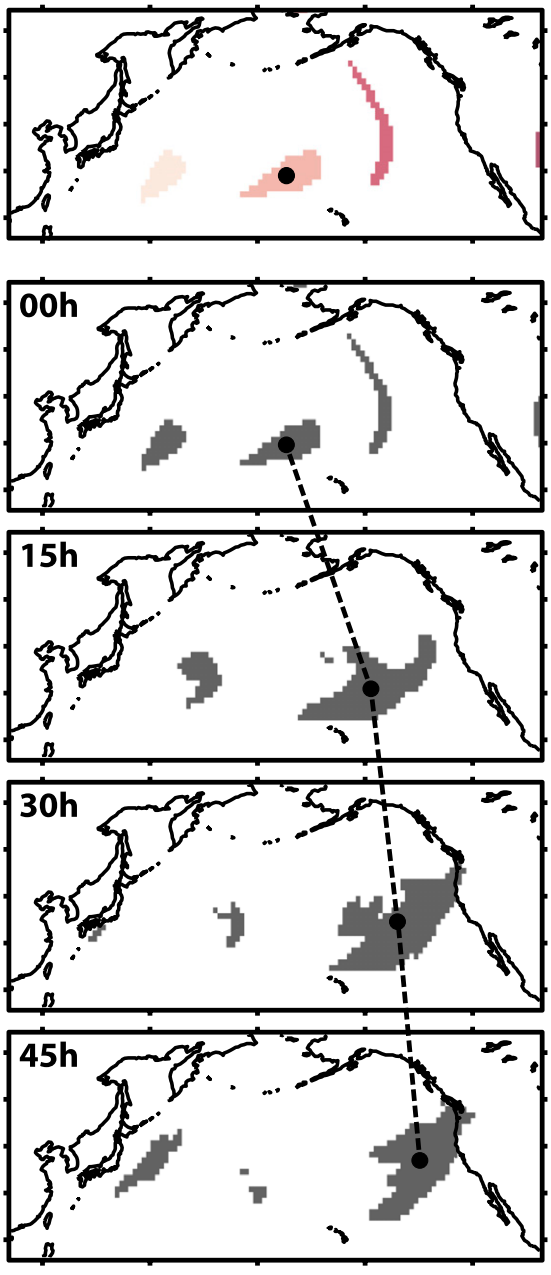

FIG. 3. An example of the tracking algorithm applied to 1800 UTC 1 Dec 2007. Separated features are colored in varying shades of pink and the centroid of the AR of interest is marked by a filled black dot. Starting from 1800 UTC 1 Dec 2007, the AR of interest is tracked through time, 00–45 h as indicated by the dashed black lines.

further development because centroid locations attributed to each AR were at times inconsistent. Our criteria for linking centroids over time is as follows. 1) The centroid of the tracked feature at landfall must correspond to the selected landfalling date chosen using the methods described in the previous subsection. 2) The general progression of centroids should be eastward. There is some east–west jumping in centroid location associated with the addition of remnant moisture to the selected feature, but it is quite minor compared to the overall progression of the feature in time. 3) The centroid of the westernmost feature is selected when two features merge (this can be seen between the 00 and 15 h time steps in Fig. 3).

For the 112 AR events tracked using our algorithm, we rank the events in order of weakest to strongest according to each AR's lifetime average of the areal maximum MF recorded at each time step. This ranking system takes into account the entire AR lifetime rather than only its landfalling intensity and allows us to compare and contrast quantitatively the weakest and strongest ARs in the subset. The lifetime average intensities range from 533 to 1001 kg m^{-1} s^{-1}. It should be emphasized here that ARs are by definition extreme events and that the "weak" ARs we refer to in our data subset are those selected ARs with the lowest lifetime average of maximum MF.

c. *Composites*

All composites in our study are calculated based on the longitudinal position of the AR centroid at each time step, as regionally centered composites. The gray boxes in the following figures mark out four regions: 1) 175°–160°W, 2) 160°–145°W, 3) 145°–130°W, and 4) 130°–115°W. For each AR, variables are first averaged for all centroid values within a given region prior to calculating the composite to avoid double-counting slowly moving ARs. Even though many of the trajectories for the tracked ARs extend over the western Pacific, we limit our composites to the eastern Pacific (the four regions listed above) to avoid oversampling the longest-lived ARs.

d. *Rossby wave breaking and diagnosis*

Rossby wave breaking (RWB) is defined as the rapid and irreversible overturning of potential vorticity (PV) contours (McIntyre and Palmer 1983). Rossby waves propagate along a strong PV gradient and break when the gradient is weakened, such as in a jet exit region. For composites we use PV on the 200-hPa surface to detect breaking and determine the type of breaking: anticyclonic, in which contours overturn in the southwest–northeast direction, or cyclonic, in which contours overturn in the northwest–southeast direction. Breaking type is determined on a case by case basis based on breaking direction (see Fig. 1 in Strong and Magnusdottir 2008b). The impact of the breaking events is on forcing of the background flow, often determined to be greater when the spatial scale of the breaking is greater.

The location and zonal extent of each breaking event is quantified using a RWB detection algorithm first described in Strong and Magnusdottir (2008b) and adapted to 3-hourly MERRA PV data at 200 hPa (coarsened to a resolution of 2.5° × 2.5° using linear interpolation). With this method, the Northern Hemisphere 200-hPa PV field is divided into 400 bins of equal area of approximately $6.4 \times 10^5\,\mathrm{km}^2$. For each 3-h time step, we identify the longest circumpolar PV contour considering all contours between 0 and 20 PVU [at an interval of 0.5 PVU; 1 potential vorticity unit (PVU) ≡ $10^{-6}\,\mathrm{m}^2\,\mathrm{s}^{-1}\,\mathrm{K}\,\mathrm{kg}^{-1}$]. If overturning is detected (contour crosses a meridian more than once), the centroid of the breaking "bay" and zonal extent (L, calculated as the degree arc length of a great circle passing through the centroid and spanning the breaking bay) and contour on which the breaking is detected are recorded [for details, see the appendix in Strong and Magnusdottir (2008b)]. For each bin centered on (λ, ϕ) and numbered $n = 1, \ldots, N$, the relative frequency of breaking (γ) and mean zonal extent of breaking ($\overline{L}$) are calculated as follows:

$$\gamma(\lambda,\phi)_n \equiv \frac{1}{T}\sum_{t=1}^{T}\beta[(\lambda,\phi)_n, t] \quad \text{and} \tag{2}$$

$$\overline{L}(\lambda,\phi)_n \equiv \frac{1}{\sum_{t=1}^{T}\beta}\sum_{t=1}^{T}L[(\lambda,\phi)_n, t], \tag{3}$$

where

$$\beta[(\lambda,\phi)_n, t] = \begin{cases} 1 & \text{if centroid is present} \\ 0 & \text{otherwise} \end{cases} \tag{4}$$

and T is the total number of 3-hourly observations. For each type of breaking (anticyclonic and cyclonic), γ quantifies the spatial frequency of breaking for a given time period, where areas of high breaking frequency typically overlap areas of large zonal extents.

4. Characteristics of ARs at landfall

a. Climatology for extended winter

First, we consider the landfalling characteristics of ARs off the west coast of North America using daily averages for the extended winter (November–March) 1979–2011. Landfall is defined as physical proximity to land, as shown in Fig. 1a. As described in section 3b, our climatology of landfalling ARs is composed of all dates for which at least three grid points in the zonal direction, within the boxed region of Fig. 1, have peak daily MF values greater than a set threshold based on the 85th percentile. Of the 4992 dates in the entire time period, 749 are retained as landfalling AR dates. Of the 128 AR dates listed in the climatology in Neiman et al. (2008b), 77 are contained in our climatology and an additional 16 occur in close proximity (less than or equal to ±2 days) to dates in our climatology. Moreover, a number of ARs identified in our study are not included in the Neiman climatology. Differences between the two climatologies are likely attributable to different definitions of AR landfall and the use of moisture flux rather than integrated water vapor, as was used in Neiman et al. (2008b). The 749 dates contain all of the most recent notable landfalling AR events (seen in Fig. 2).

The largest number of landfalling dates occur early in the season. An average of 6.1 landfalling dates occurred in November (202 dates total), 5.8 in December (192 dates total), 5.2 in January (179 dates total), 3.2 in February (110 dates total), and 1.9 in March (67 dates total). The decrease in the number of landfalling dates over the course of the season is in general agreement with the findings in Neiman et al. (2008b, see their Fig. 2), which are based on observations of Special Sensor Microwave Imager (SSM/I) integrated water vapor plumes for 1998–2005.

Figure 4a shows the seasonal breakdown of landfalling latitude. Landfalling latitudes show a shift equatorward toward the end of the season, from an average latitude in November of 45.6°N to a March average of 42.2°N. This shift is also seen in landfalling peak daily MF (Fig. 4b). The most intense landfalling AR dates occur in the month of November ($302.3\,\mathrm{kg}\,\mathrm{m}^{-1}\,\mathrm{s}^{-1}$) and the weakest occur in the month of March ($283.6\,\mathrm{kg}\,\mathrm{m}^{-1}\,\mathrm{s}^{-1}$). While associated landfalling total daily precipitation does not show a similar trend (Fig. 4c), precipitation anomalies (based on the daily climatology) show a shift equatorward over the course of the season (not shown).

b. Effects of the MJO and ENSO on ARs

We perform an analysis of the roles of ENSO and the MJO in modulating ARs at landfall using the MEI and RMM indices, respectively. While these large-scale patterns certainly influence the precipitation distribution in the western United States (Ropelewski and Halpert 1987; Cayan et al. 1999; Higgins et al. 2000; Jones 2000), our purpose here is to investigate whether they play a direct role in AR behavior at landfall. In our analysis of the MJO, we limit our investigation to amplitudes of the MJO index greater than 1, reducing the number of dates from 749 to 469 landfalling AR dates.

The largest number of landfalling dates occur during El Niño (301 dates) and the fewest during La Niña (180 dates), with 268 landfalling dates occurring during ENSO neutral conditions. Figures 4d and 4e show the breakdown of landfalling latitude, intensity, and precipitation

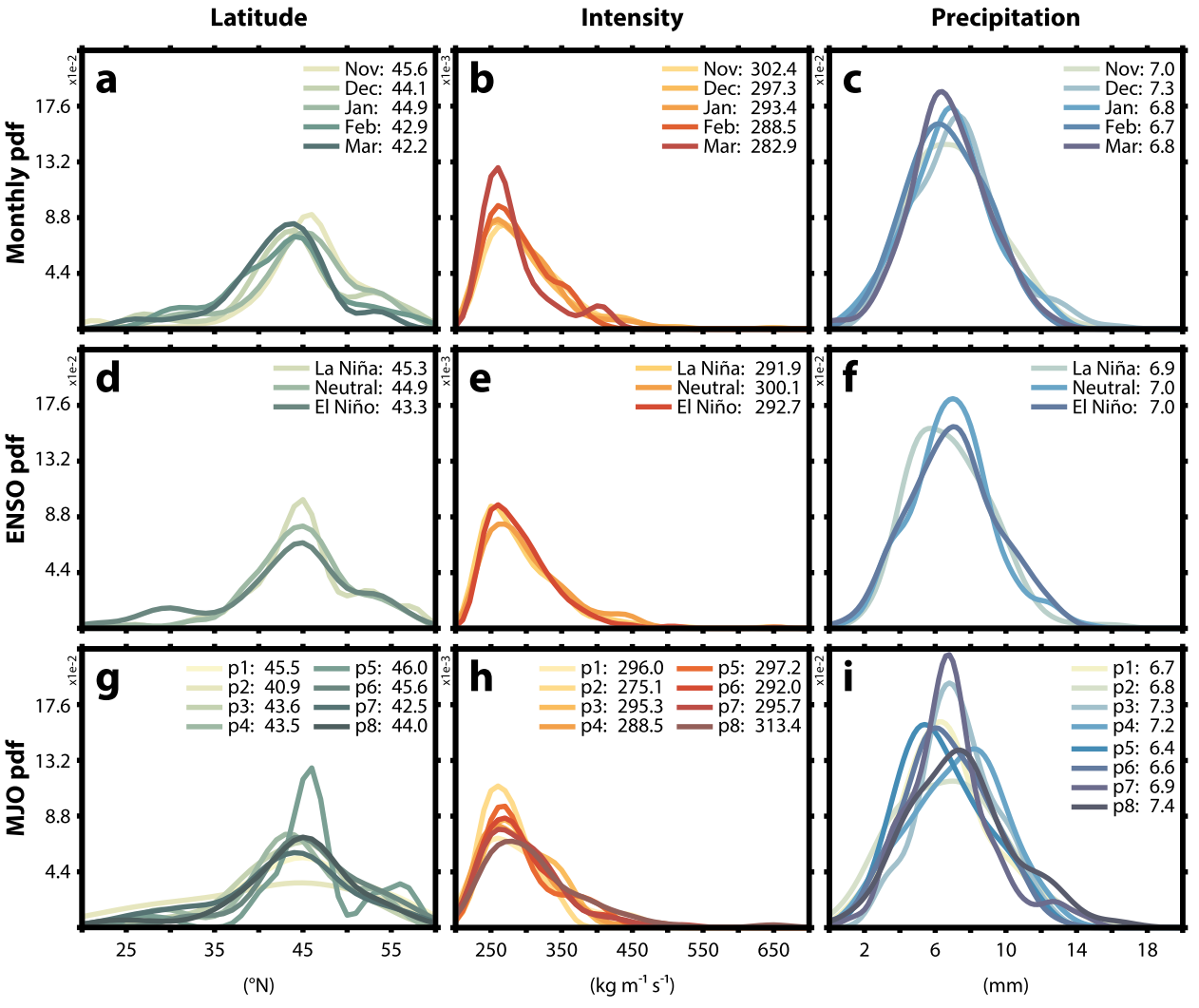

FIG. 4. Probability density functions for landfalling ARs over the extended winter for the years 1979–2011 sorted according to (a)–(c) month (749 dates), (d)–(f) ENSO phase (749 dates), and (g)–(i) MJO phases with amplitudes greater than one (469 dates). Each column shows the distribution of (left) landfalling latitude, (center) landfalling peak daily MF, and (right) landfalling total daily precipitation. The *y* axis shows the probability density function for each panel, where the center column is an order of magnitude less than the right and left columns. Averages for each category are shown in the legend of each panel.

by phase of ENSO. Landfalling latitudes during El Niño events are shifted equatorward, with an average latitude of 43.3°N compared to an average latitude of 45.5° and 44.9°N for La Niña and neutral phases, respectively. While total precipitation remains similar (Fig. 4f), the poleward shift in landfalling latitude during La Niña events and concentration of positive precipitation anomalies in the Pacific Northwest (not shown) is consistent with wintertime precipitation patterns for the region during La Niña (NOAA/Climate Prediction Center). Increased intensity of moisture plumes during ENSO neutral landfalling dates is consistent with previous findings (Higgins et al. 2000; Bao et al. 2006). Landfalling intensities for El Niño and La Niña dates show little difference (Fig. 4e).

Figure 5 shows the composite anomalies of 200-hPa zonal wind (dark gray contours) and PV (light gray contours), and the composite anomalies of MF (shaded) for each phase of ENSO. Anomalies are calculated from the daily climatology for each variable and only significant MF anomalies are shown (calculated at the 95% level using a Student's *t* test). Comparison of Figs. 5a and 5c shows a clear equatorward shift in the zonal wind during El Niño dates that is in agreement with Fig. 4d. Significant MF anomalies during El Niño dates cover the entire coastline from Mexico to Alaska. The significant composite anomaly does not extend south of 35°N during La Niña and neutral dates. Warm phase positive precipitation anomalies mirror the meridionally

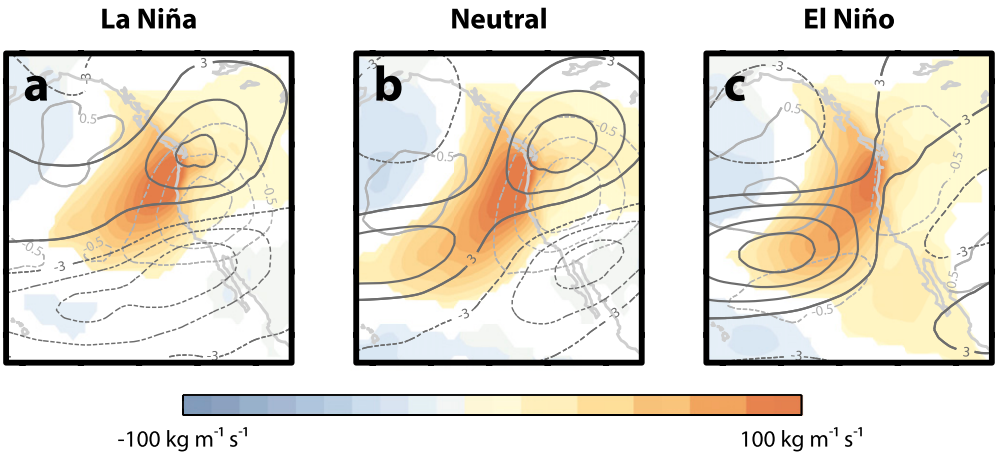

FIG. 5. Composite 200-hPa zonal wind anomalies (dark gray contours, intervals of 3 m s^{-1}), 200-hPa PV anomalies (light gray contours, intervals of 0.5 PVU), and MF anomalies (shaded, intervals of 10 kg m^{-1} s^{-1}), with negative contours dashed, for (a) La Niña (180 dates), (b) neutral (268 dates), and (c) El Niño (301 dates), for all 749 ARs over the extended winter in years 1979 to 2011 (15°–65°N, 160°–115°W). Anomalies are calculated from the daily climatology of each variable. Only statistically significant anomalies are depicted. Statistical significance is calculated using Student's *t* test at the 95% level.

extended range of MF anomalies (not shown), consistent with wintertime precipitation patterns during El Niño (NOAA/Climate Prediction Center). The most noticeable difference between the different parts of Fig. 5 is in the zonal wind anomalies. El Niño landfalling dates are associated with an equatorward shifted jet. This suggests that the major role ENSO plays in modulating landfalling ARs is through influence on the position of the jet, which affects the location of the Rossby wave breaking region, as will be discussed in section 4c.

Figures 4g–i show the breakdown of landfalling latitude, intensity, and precipitation by phase of the MJO. There are two local maxima in the overall number of landfalling AR dates by phase (not shown). The largest number of landfalling AR dates occur during phase 6 (84 dates) and increased activity in phases 7 and 8 (71 dates each), and a smaller secondary peak occurs at phase 3 (62 dates). The peak in AR activity in association with phase 3 (when tropical convection is over the Indian Ocean) and the phase 7–8 increases are consistent with findings in Jones (2000). The peak at phase 6 is consistent with the increase in AR activity described in Guan et al. (2012). While there is no clear trend in landfalling latitude, phases 2 and 5 have the most extreme equatorward (40.9°N) and poleward (46.0°N) mean landfalling latitudes, respectively (Figs. 4a,d,g). The two peaks in the number of landfalling AR dates are approximately reflected in precipitation totals, with phase 3 showing the largest average at 7.3 mm and phase 5 showing the smallest average at 6.4 mm (Fig. 4i), consistent with wintertime precipitation patterns for the western United States (NOAA/Climate Prediction Center).

Figure 6 shows 200-hPa zonal wind (dark gray contour) and PV (light gray contour) composite anomalies, and MF (shaded) composite anomalies for each phase of the MJO, showing only statistically significant MF anomalies. We find that positive precipitation anomalies shift approximately poleward from phase 1 to phase 8 (not shown), with the exception of phases 2 and 7. While all phases of the MJO show the presence of a statistically significant moisture anomaly, the anomaly for phase 2 is weak and spread out. It reaches the farthest equatorward, consistent with the very low landfalling latitude and low intensity shown for phase 2 in Figs. 4g and 4h. The largest positive MF anomaly is in phase 7, which shows the presence of strong equatorward zonal wind anomalies very similar to Fig. 5c, the El Niño composite. Phase 8, which has the largest landfalling intensity and precipitation total from Figs. 4h and 4i, also shows eastward extended zonal wind anomalies, consistent with higher-latitude positive precipitation anomalies (not shown). MJO phases 3 and 7 have similar landfalling latitudes, intensities, and precipitation patterns (not shown).

A strong common characteristic of AR composites during ENSO and MJO phases is the presence of a perturbed PV field in the eastern Pacific, in the location of the jet exit region, as indicated by the negative PV anomalies centered over the coastline in Figs. 5 and 6. The composites in this section suggest that, while ARs may be modulated by tropical influences on the extratropics,

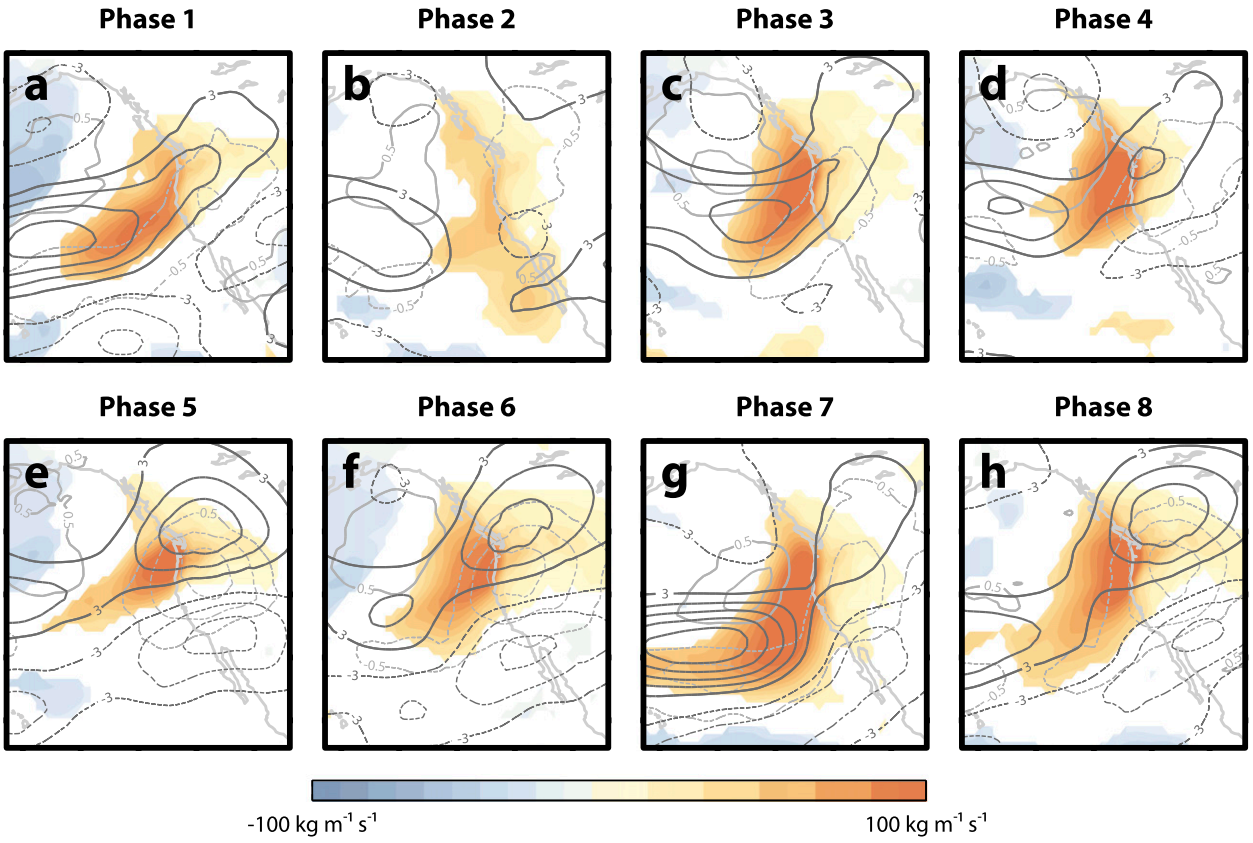

FIG. 6. As in Fig. 5, but for the MJO, for (a) phase 1 (38 dates), (b) phase 2 (49 dates), (c) phase 3 (62 dates), (d) phase 4 (43 dates), (e) phase 5 (51 dates), (f) phase 6 (84 dates), (g) phase 7 (71 dates), and (h) phase 8 (71 dates), for all 469 ARs over the extended winter in the years 1979–2011 with RMM amplitudes greater than 1 (15°–65°N, 160°–115°W).

AR variability is ultimately strongly tied to extratopical dynamical mechanisms. This common characteristic motivates our investigation of the dynamical mechanisms modulating ARs.

c. *Dynamical perspective*

We consider how landfalling AR dates are different from the mean state. Figure 7 shows composite sea level pressure (SLP), 200-hPa PV, 200-hPa wind speed, and MF for each winter month for the entire period (1979–2011) irrespective of peak daily MF (Figs. 7a–e), all 749 landfalling AR dates (dates with values above the 85th percentile of peak daily MF; Figs. 7f–j), and all 112 selected AR dates (dates with values above the 95th percentiles of peak daily MF and associated total daily precipitation; Figs. 7k–o). Composites in Figs. 7f–j are composed of 202, 191, 179, 110, and 67 individual dates, respectively. Composites in Figs. 7k–o are composed of 34, 31, 27, 14, and 6 individual dates, respectively.

Comparison of the bottom two rows of Fig. 7 with the top row shows a striking departure in the dynamical makeup of AR dates from the climatological mean state over the eastern Pacific in terms of Rossby wave dynamics. The top row shows an unperturbed jet, with an associated largely zonal PV field and unremarkable MF. For each month (each column), the two AR rows show that associated with the strong, lower-tropospheric MF (which defines the ARs), the PV field and the jet are deformed to a varying extent, manifesting that Rossby wave breaking is taking place. While each frame is an average over many cases, one can still see evidence of overturning PV contours and thus Rossby wave breaking (or nonlinear Rossby wave behavior).

All AR dates (the middle and bottom rows of Fig. 7) are associated with a westward retreated jet, large perturbations in the PV field, and a clearly defined low pressure center to the north and a weak high pressure center to the south of the jet. The jet is climatologically in its most poleward position in November and shifts equatorward over the course of the season. This shift in the jet is reflected in the equatorward shift in landfalling latitude shown in Fig. 4a. Retreat of the jet maximum westward over the course of the season weakens the PV gradient and allows for distortion of the PV contours in

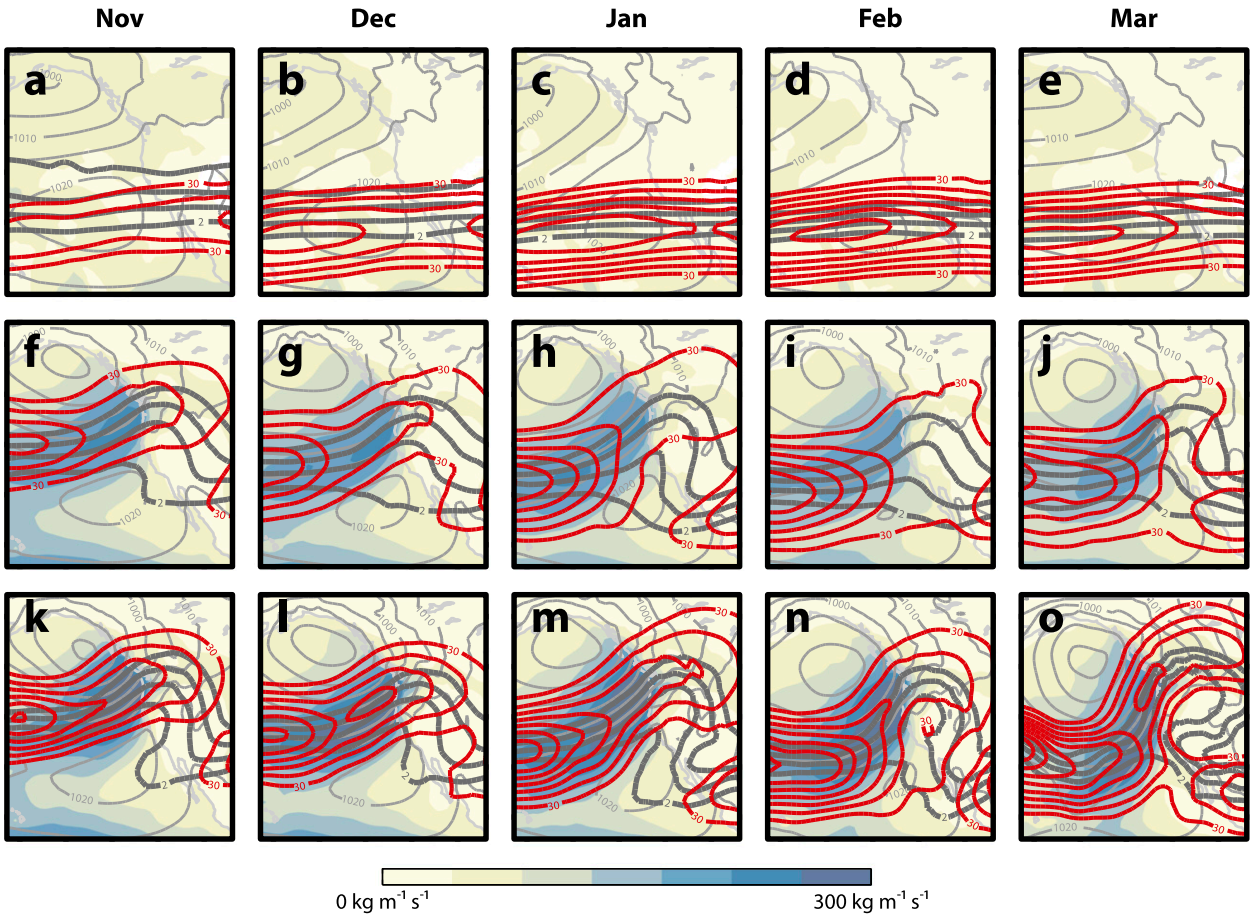

FIG. 7. Composite SLP (light gray contour, intervals of 5 hPa), PV at 200 hPa (dark gray contour, intervals of 1 PVU), wind speed at 200 hPa (red contour, intervals of 5 m s^{-1}), and MF (shaded) for (from left to right) November, December, January, February, and March for (a)–(e) the climatological mean of the extended winter over the years 1979 to 2011, (f)–(j) all 749 ARs over the extended winter in the years 1979 to 2011 and (k)–(o) the 112 selected landfalling dates (15°–65°N, 160°–115°W).

the eastern Pacific. The reduction in the PV gradient is downstream and equatorward of the jet exit region. The relationship between the jet and PV field in the monthly composites is consistent with the findings outlined in Abatzoglou and Magnusdottir (2006; see their Figs. 5a,b).

Comparing the extreme subset of tracked AR dates (Figs. 7k–o) to all AR dates (Figs. 7f–j), we find that, consistent with the climatology, November has the largest number of ARs with 34 events and March has the lowest number with only 6 events. Unlike the climatology, however, the shift equatorward in landfalling latitudes is not apparent (not shown). All months of the extreme subset show evidence of a strongly perturbed jet maximum and breakdown of the PV gradient in the eastern Pacific, both in association with the curvature of the moisture plume close to the surface toward the coastline (Figs. 7k–o). For the extreme subset of ARs (bottom row of Fig. 7), all months show a close relationship between the moisture plume at lower levels and the jet maximum at upper levels. This strong, yet deformed, jet is associated with increased distortion of the PV contours and anticyclonic breaking over all months. While there are no discernible changes in the strength of the high pressure center to the south of the moisture plume, the selected ARs have a much deeper low pressure center to the north.

d. Composites of selected cases over the basin

Moving away from static composites of ARs at landfall, we consider the variability of ARs over the Pacific and their development prior to landfall. Figure 8a shows trajectories, smoothed using a moving average filter, for all 112 ARs selected, colored according to their lifetime intensity. Figure 8b shows the relation of initial longitudinal locations in the extratropics relative to the four regions designated in Fig. 8a (the *y* axis has no significance), again colored according to their lifetime intensity. The AR trajectories lie approximately equatorward of

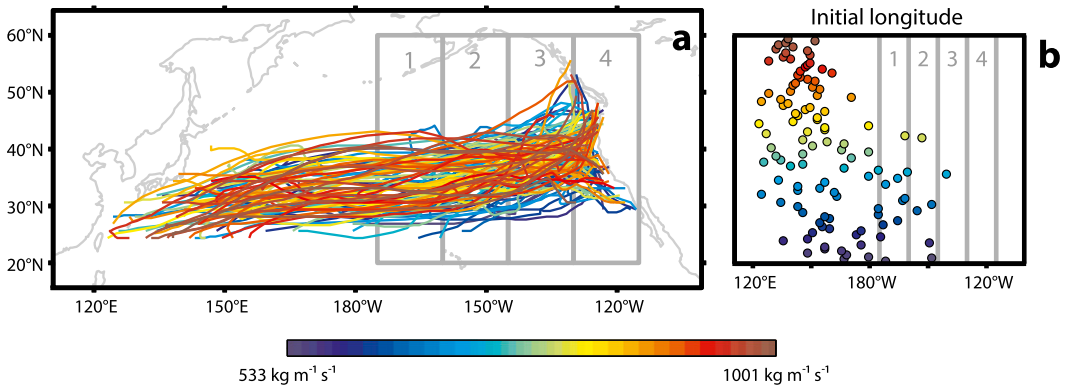

FIG. 8. (a) Trajectories of all 112 landfalling AR cases, shaded according to lifetime intensity (as described in section 3). The gray boxes in (a) and (b) refer to the same areas and represent the regions over which composites are calculated based on AR centroid location: 1) 175°–160°W, 2) 160°–145°W, 3) 145°–130°W, and 4) 130°–115°W. (b) Each point represents the longitude at which the AR is first detected.

the storm track over the Pacific, consistent with their association with the warm sector of extratropical cyclones [based on visual comparison with Fig. 1 in Hoskins and Valdes (1990)]. The strongest ARs have initial locations primarily in the western Pacific and the weakest ARs have initial locations generally located more eastward (Fig. 8b).

Using the centroid information recorded for each AR, we investigate the nature of the relationship between Rossby waves in the upper troposphere and ARs in the lower troposphere. Figure 9 shows the composite time evolution of the 200-hPa PV field (dark gray contours), 200-hPa wind speed (red contours), SLP (light gray contours), and MF (shading). The red filled circle indicates the average AR centroid location for each composite. The first two frames of the figure (Figs. 9a,b) depict, in the PV field, the eastward propagation of the Rossby wave with the AR centroid following closely. By Fig. 9c, there is evidence of RWB, which becomes clearer in Fig. 9d in terms of the perturbed PV field. Mirroring the behavior of the PV field and the jet in the eastern Pacific, MF curves poleward just off the coast of North America (Figs. 9c,d).

It is important to note that Fig. 9 is a composite over many cases, which will lead to a smoothing out of the PV field. On a case by case basis, the ARs at landfall are typically positioned along the western edge of a breaking bay over the eastern Pacific and terminate prior to complete overturning of the PV contours. For most of the cases investigated, the resulting breaking is anticyclonic in nature, apparent in Fig. 9d (although diluted due to averaging). The location of breaking associated with the ARs is consistent with both the position of the ARs on the equatorward (anticyclonic) side of the jet and the wintertime RWB climatology for anticyclonic breaking over the Pacific, downstream of the jet maximum (Strong and Magnusdottir 2008b).

5. Intensity differences in selected cases

To illustrate the dynamical differences that contribute to variations in AR intensity over the basin in greater detail, we divide our subset of extreme AR events into two groups according to average lifetime intensity. Dates with lifetime intensities exceeding the 90th percentile were chosen as our top dates (11 total with values greater than 858.9 $\mathrm{kg\,m^{-1}\,s^{-1}}$) and dates falling below the 10th percentile were chosen as our bottom dates (11 total with values less than 612.6 $\mathrm{kg\,m^{-1}\,s^{-1}}$). Composites for these two groups in the following figures are based on the position of the AR centroid, as in Fig. 9, with strong AR composites on the left and weak AR composites on the right.

a. Composites

Figure 10 shows the composited time evolution of the 200-hPa PV field (dark gray contours), 200-hPa wind speed (red contours), SLP (light gray contours), and MF (shading) of the 11 strongest (Figs. 10a–d) and 11 weakest ARs (Figs. 10e–h).

The progression of the strongest ARs is associated with a sustained upper-level jet, even as RWB is taking place, with a deep low pressure center to the north and a well-defined and persistent high pressure center to the south (Figs. 10a–d). MF plumes have values in excess of 400 $\mathrm{kg\,m^{-1}\,s^{-1}}$ and are well supported throughout their lifetime by a strong, collocated upper-level jet. Progression eastward is associated with increased nonlinear behavior in the PV field (overturning of contours in Figs. 10b–d). In Fig. 10d, anticyclonic overturning of PV

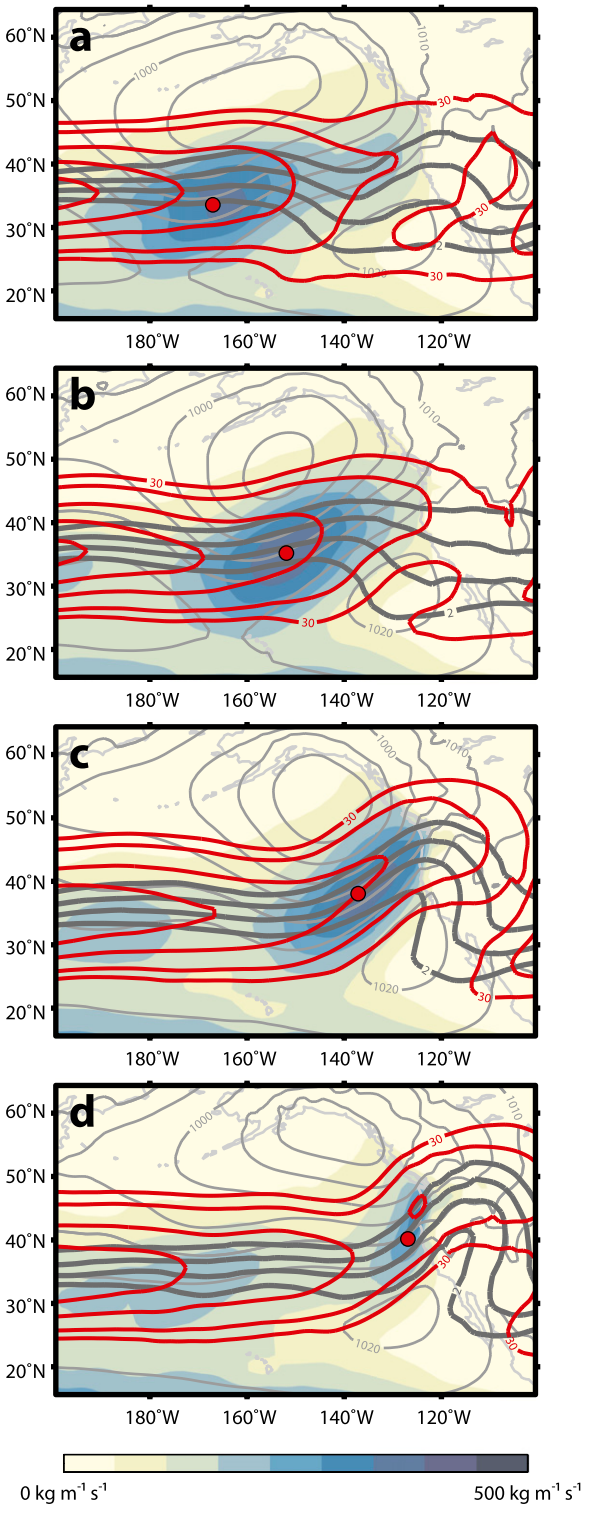

FIG. 9. Composite SLP (light gray contour, intervals of 5 hPa), PV at 200 hPa (dark gray contour, intervals of 1 PVU), wind speed at 200 hPa (red contour, intervals of 10 m s^{-1}), and MF (shaded) for the 112 AR events in our extreme subset for (a) 175°–160°W, (b) 160°–145°W, (c) 145°–130°W, and (d) 130°–115°W. The average location of the AR centroid is marked by a filled red dot.

contours is apparent around 120°W and is concurrent with weakening of the AR plume.

Relative to the strongest ARs, the weakest ARs are associated with a weaker jet in the eastern Pacific as RWB takes place, a shallower low pressure center to the north, and the absence of a persistent high pressure center to the south (Figs. 10e–h). The associated extratropical cyclone for the strongest ARs is a much tighter system and stronger than the cyclone associated with the weakest ARs. Comparison of MF between the two groups shows the evolution of a much smaller and weaker AR, with values generally below 350 kg m^{-1} s^{-1}. The PV field remains relatively linear over the central Pacific with the appearance of the ARs. As for the strongest ARs, the weakest ARs are also preceded by breaking in the eastern Pacific around 120°W. Development of nonlinear behavior in the PV field over the eastern Pacific with AR propagation is delayed and it is less coherent and not as well defined compared to features in the left column (Figs. 10g,h).

Both the weakest and strongest ARs are associated with the formation of anticyclonic breaking in the eastern Pacific. However, in the weakest ARs, this effect is muted in the composite and appears later in their life cycle (Fig. 10h). While ARs developing in association with linear Rossby wave propagation were observed, none had intense enough moisture transport off the coast of North America to fit into our extreme subset.

b. *Rossby wave breaking*

To examine the influence that each type of RWB has on AR intensity, we compare the locations and characteristics of RWB for the strongest and weakest ARs. In general, ARs are much more strongly associated with anticyclonic breaking than cyclonic breaking, especially over the eastern Pacific (i.e., Fig. 10). Cyclonic breaking associated with the progression of ARs over the basin and at landfall is dispersed relative to the location of the AR centroids (not shown). The weakest ARs are associated with an increase in the frequency of cyclonic RWB in the eastern Pacific relative to the strongest ARs (not shown). However, the average zonal extent of cyclonic breaking for both groups generally decrease as the ARs progress into the eastern Pacific. We focus on the influence of anticyclonic RWB on AR intensity for the remainder of this section.

To illustrate the influence of anticyclonic breaking on ARs, we investigate the breaking locations in relation to the average position of the AR centroid for the strongest and weakest ARs. Each row of Fig. 11 shows all anticyclonic breaking events that occur simultaneously with the centroid in the region outlined in black (both within the region and east of the region). The sizes of the colored

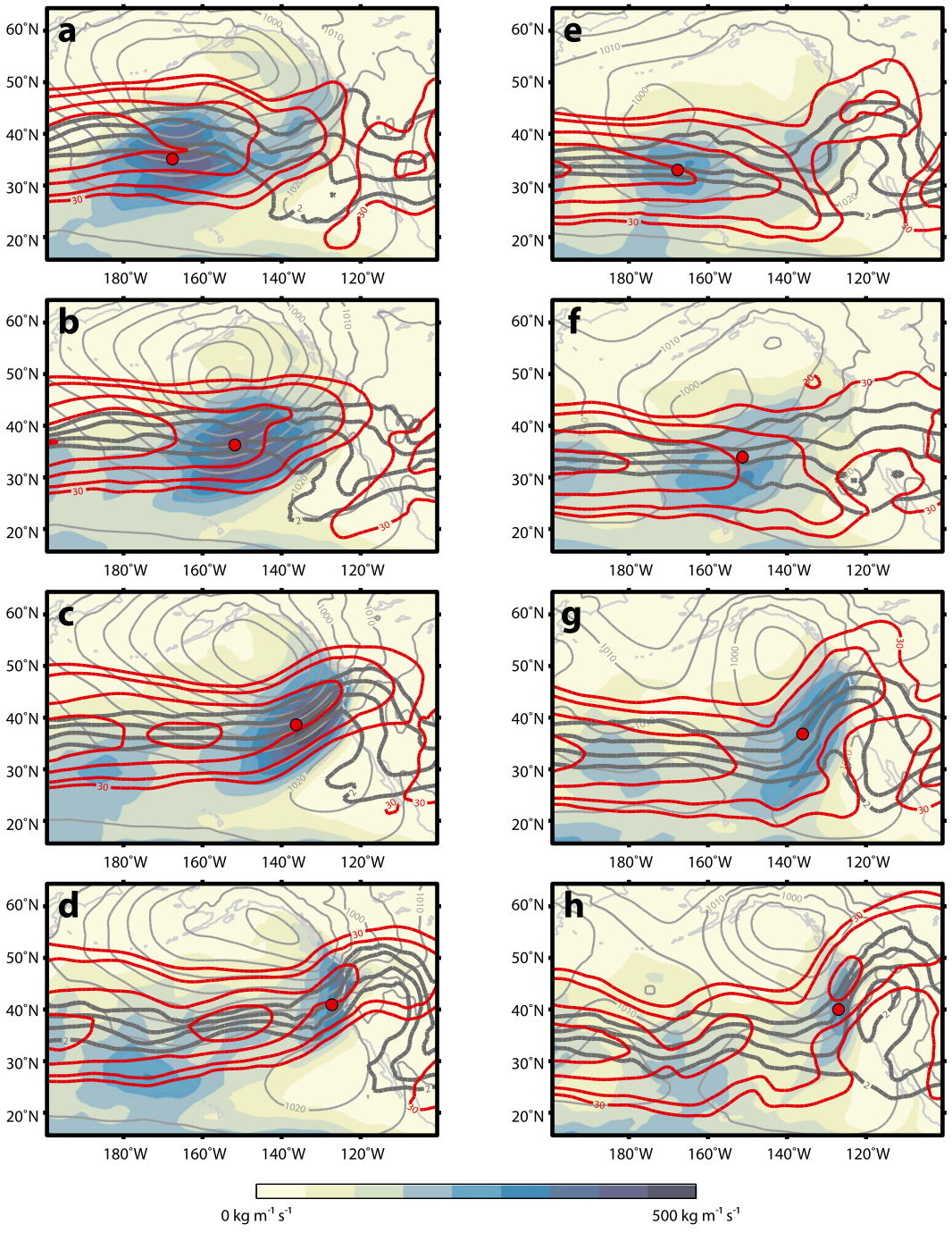

FIG. 10. As in Fig. 9, but for the (left) 11 strongest and (right) 11 weakest ARs in our extreme subset for (a),(e) 175°–160°W, (b),(f) 160°–145°W, (c),(g) 145°–130°W, and (d),(h) 130°–115°W. The average location of the AR centroid is marked by a filled red dot.

markers are scaled according to the zonal extent of each breaking event. The shading of the markers indicates the PV contour on which overturning is detected in units of PVU. At 200 hPa, breaking is generally detected between 0.5 and 8 PVU, consistent with breaking recorded for the 350-K level in Strong and Magnusdottir (2008b).

The strong association of ARs with anticyclonic RWB is consistent with position of ARs on the equatorward side of the jet and the location of the wintertime anticyclonic surf zone in the eastern Pacific (Abatzoglou and Magnusdottir 2006; Strong and Magnusdottir 2008b). For the strongest ARs, anticyclonic breaking is almost

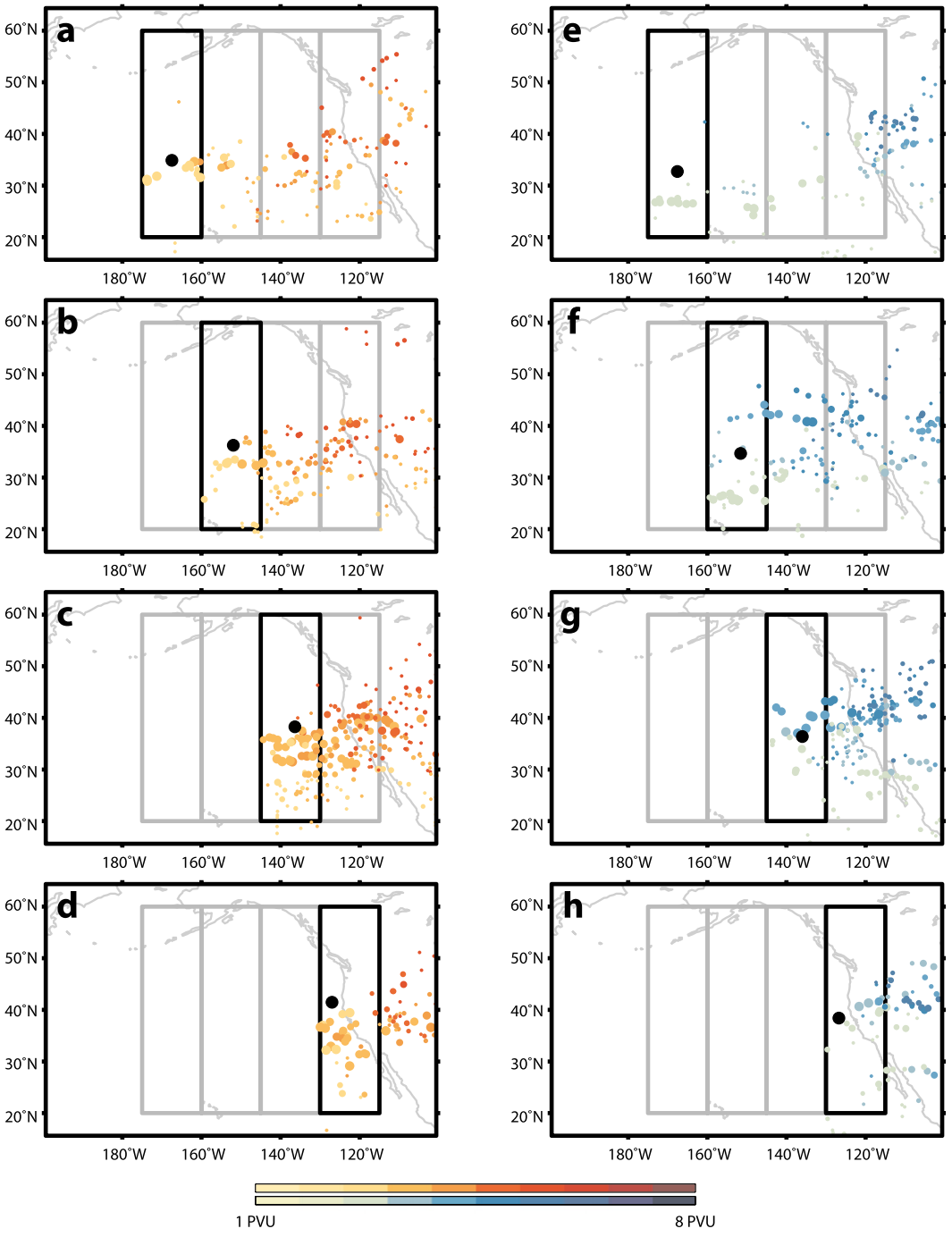

FIG. 11. Relationship between the location of the AR (filled black dot) and anticyclonic RWB for the (a)–(d) 11 strongest and (e)–(h) 11 weakest ARs. Using the same regions as in Fig. 9, for each panel, the region the AR is in is outlined in black and all breaking occurring within and leading that region is plotted, where shading indicates the position of breaking (PVU) and size indicates its zonal extent.

exclusively limited equatorward of the AR centroid and stays relatively concentrated as the AR moves eastward (Figs. 11a–d). For the weakest ARs, breaking is much more dispersed meridionally and is less concentrated (Figs. 11e–h). The overall frequency of anticyclonic breaking is slightly higher for the weakest ARs; however, there are no apparent trends in the frequency of breaking in each region for either the strongest or weakest ARs. The average zonal extents of the breaking events increase for the strongest ARs (from 9.3 to 10.6 arc length units)

and decrease for the weakest ARs (from 10.6 to 9.1 arc length units) as the AR propagates eastward. For the strongest ARs, anticyclonic RWB becomes more spatially concentrated equatorward of the AR centroid, as the AR approaches landfall (Figs. 11c,d).

c. *Anticyclonic RWB characteristics of all landfalling ARs*

We extend our results to the entire AR climatology and consider the frequency and extent of anticyclonic RWB for all landfalling AR dates compared to the RWB climatology for the extended winter. Figure 12 shows the relative frequency γ and average zonal extent $\overline{L}$ for anticyclonic RWB for the climatology for the extended winter (Fig. 12a), all landfalling AR dates (Fig. 12b), and the selected subset of extreme landfalling AR dates (Fig. 12c). Accounting for differences in the datasets and the use of the 200-hPa pressure surface, the general location of average zonal extent and breaking frequency are consistent with Strong and Magnusdottir (2008b, their Fig. 2a). Breaking events at this level are detected between 0.5 and 8 PVU, again generally consistent with the findings in Strong and Magnusdottir (2008b). Comparison of Figs. 12b and 12c with Fig. 12a shows that the maximum in anticyclonic RWB frequency is shifted eastward, over the coast, for AR dates. The strongest AR dates are associated with a substantially higher frequency of anticyclonic breaking in the eastern Pacific, located over the coastline and slightly equatorward of the relative frequency for all ARs over the time period.

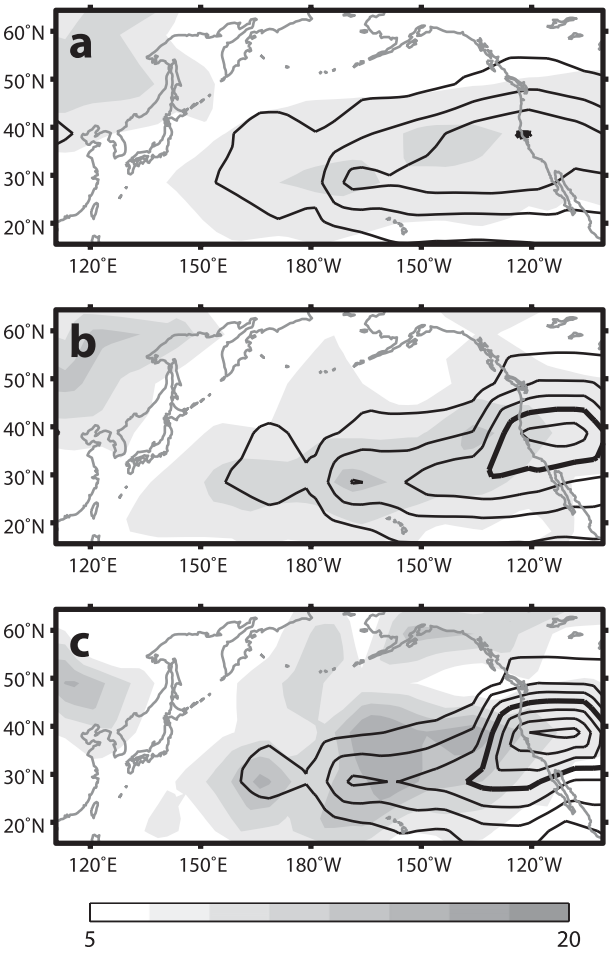

FIG. 12. Anticyclonic RWB relative frequency γ (contoured, intervals of 0.05 with the 0.2 contour thickened) and average zonal extent $\overline{L}$ (shaded, units of arc length) for (a) the climatological mean of the extended winter in the years 1979–2011, (b) all 749 landfalling AR dates over the extended winter in the years 1979–2011, and (c) the selected subset of 112 extreme landfalling AR dates.

6. Discussion and conclusions

This study uses MERRA reanalysis moisture and dynamical fields to investigate large-scale features of atmospheric rivers at landfall and the role of Rossby wave breaking in modifying their behavior and intensity over the Pacific basin prior to landfall. Landfalling ARs are identified as plumelike features in MF that are above a threshold determined by the data and in physical proximity to the coastline of North America. We investigate the general characteristics of AR landfall over the extended winter (November–March) over more than three decades (1979–2011) by setting this threshold to the 85th percentile of peak daily MF averaged over the region defined in Fig. 1a. For a more in-depth investigation, from this dataset of landfalling ARs we objectively select 112 landfalling AR dates by changing the set threshold to the 95th percentiles of peak daily moisture flux and total daily precipitation, again averaged over the region defined in Fig. 1a. The 112 AR dates include four significant AR storms that are well documented in the literature. A tracking algorithm based on MF was developed to expand each landfalling event to its full lifetime, from its first appearance in the extratropics as a persistent feature to its termination after making landfall. Use of this tracking algorithm allows for an investigation of the characteristics of each AR, specifically intensity and the path of its centroid over time.

Approximately 15% of the dates are landfalling AR days. The largest and most intense landfalling AR days occur in November, with fewer and less intense ARs later in the season. Latitude of landfall shifts equatorward, with the farthest poleward ARs occurring in November and the farthest equatorward ARs occurring in March. While there are no seasonal trends in total daily precipitation, positive precipitation anomalies shift

equatorward over the course of the season (not shown), in line with the seasonality of extreme precipitation events in the western United States (e.g., Fig. 3 in Ralph et al. 2014).

Composites of landfalling AR events show a close relationship among ARs, the 200-hPa PV field, and the closely associated 200-hPa jet. The most noticeable difference in ARs between the different phases of ENSO is in the latitude of landfall. Most landfalling AR dates occur during El Niño, and the fewest occur during La Niña. The MJO is shown to modulate the intensity of landfalling ARs, as well as precipitation totals.

While seasonality in the jet structure may influence the intensity of ARs prior to landfall, not all of the most intense ARs make landfall early in the season. Investigation of the upper-level characteristics of the extreme subset of dates tracked over the basin shows some common features, such as an extended strong jet and the formation of RWB in the eastern Pacific (Figs. 7f–j). Focusing on the behavior of the tracked ARs over the basin, the strongest ARs first appear in the extratropics in the western Pacific and their trajectories generally correspond to the equatorward side of the jet. Composites of upper-level fields following the progression of the AR eastward over the basin show a close relationship between Rossby wave activity flux and moisture flux. In general, most of the ARs studied formed in association with Rossby wave propagation in the central Pacific, eventually terminating as anticyclonic RWB took place in the eastern Pacific.

We focus on the dynamical differences influencing AR intensity prior to landfall by comparing the strongest dates to the weakest dates in our subset, determined based on the 90th and 10th percentiles of the lifetime intensity of all 112 tracked ARs, respectively. The differences in the strongest and weakest ARs are apparent in the development and extent of anticyclonic RWB in the eastern Pacific. The strongest ARs are associated with a well-developed anticyclonic breaking "bay" in the eastern Pacific, a strong but highly perturbed jet, a tight low pressure center to the north or northwest, and a persistent high pressure center to the south or southeast. The weakest ARs are associated with less extensive RWB that occurs later in the lifetime of the AR, a less perturbed jet, a shallower low pressure center to the north, and the absence of a persistent high pressure center to the south.

What emerges from this study is the clear dominant influence of extratropical dynamics in terms of Rossby wave propagation and Rossby wave breaking over the eastern Pacific on the existence of landfalling West Coast ARs. ARs are associated with strong anticyclonic RWB over the eastern Pacific. This is a dynamically robust region of the world where anticyclonic RWB has been shown to lead to a positive polarity of the North Atlantic Oscillation far downstream (Strong and Magnusdottir 2008a).

Our results present a physical link between the large-scale climate patterns and ARs over the North Pacific. Previous studies have alluded to a connection between climate patterns and ARs based on correlations between signatures of ARs on land and climate pattern indices. The physical link is the process of RWB that takes place on a similar time scale as the AR lifetime. We have shown a direct link between RWB and ARs. Thus we conclude that the way in which ARs are modulated by extratropical climate patterns is driven by the interaction of these climate patterns with RWB (Strong and Magnusdottir 2008a; Rivière 2010).

Acknowledgments. We thank the two anonymous reviewers who contributed valuable comments and suggestions to improve the manuscript. This work is supported by NSF Grant AGS-1206120 and NSF GRF under Grant DGE-1321846.

REFERENCES

Abatzoglou, J. T., and G. Magnusdottir, 2006: Planetary wave breaking and nonlinear reflection: Seasonal cycle and interannual variability. *J. Climate,* **19,** 6139–6152, doi:10.1175/JCLI3968.1.

Bao, J.-W., S. A. Michelson, P. J. Neiman, F. M. Ralph, and J. M. Wilczak, 2006: Interpretation of enhanced integrated water vapor bands associated with extratropical cyclones: Their formation and connection to tropical moisture. *Mon. Wea. Rev.,* **134,** 1063–1080, doi:10.1175/MWR3123.1.

Cayan, D. R., K. T. Redmond, and L. G. Riddle, 1999: ENSO and hydrologic extremes in the western United States. *J. Climate,* **12,** 2881–2893, doi:10.1175/1520-0442(1999)012<2881:EAHEIT>2.0.CO;2.

Dettinger, M. D., 2013: Atmospheric rivers as drought busters on the U.S. West Coast. *J. Hydrometeor.,* **14,** 1721–1732, doi:10.1175/JHM-D-13-02.1.

——, F. M. Ralph, T. Das, P. J. Neiman, and D. R. Cayan, 2011: Atmospheric rivers, floods and the water resources of California. *Water,* **3,** 445–478, doi:10.3390/w3020445.

Guan, B., N. P. Molotch, D. E. Waliser, E. J. Fetzer, and P. J. Neiman, 2010: Extreme snowfall events linked to atmospheric rivers and surface air temperature via satellite measurements. *Geophys. Res. Lett.,* **37,** L20401, doi:10.1029/2010GL044696.

——, D. E. Waliser, N. P. Molotch, E. J. Fetzer, and P. J. Neiman, 2012: Does the Madden–Julian oscillation influence wintertime atmospheric rivers and snowpack in the Sierra Nevada? *Mon. Wea. Rev.,* **140,** 325–342, doi:10.1175/MWR-D-11-00087.1.

——, N. P. Molotch, D. E. Waliser, E. J. Fetzer, and P. J. Neiman, 2013: The 2010/2011 snow season in California's Sierra Nevada: Role of atmospheric rivers and modes of large-scale variability. *Water Resour. Res.,* **49,** 6731–6743, doi:10.1002/wrcr.20537.

Higgins, R. W., J.-K. E. Schemm, W. Shi, and A. Leetmaa, 2000: Extreme precipitation events in the western United States related to tropical forcing. *J. Climate,* **13,** 793–820, doi:10.1175/1520-0442(2000)013<0793:EPEITW>2.0.CO;2.

Hoskins, B. J., and P. J. Valdes, 1990: On the existence of storm-tracks. *J. Atmos. Sci.,* **47,** 1854–1864, doi:10.1175/1520-0469(1990)047<1854:OTEOST>2.0.CO;2.

Jiang, T., and Y. Deng, 2011: Downstream modulation of North Pacific atmospheric river activity by East Asian cold surges. *Geophys. Res. Lett.,* **38,** L20807, doi:10.1029/2011GL049462.

Jones, C., 2000: Occurrence of extreme precipitation events in California and relationships with the Madden–Julian oscillation. *J. Climate,* **13,** 3576–3587, doi:10.1175/1520-0442(2000)013<3576:OOEPEI>2.0.CO;2.

Lavers, D. A., G. Villarini, R. P. Allan, E. F. Wood, and A. J. Wade, 2012: The detection of atmospheric rivers in atmospheric reanalyses and their links to British winter floods and the large-scale climatic circulation. *J. Geophys. Res.,* **117,** D20106, doi:10.1029/2012JD018027.

Lynott, R. E., and O. P. Cramer, 1966: Detailed analysis of the 1962 Columbus Day windstorm in Oregon and Washington. *Mon. Wea. Rev.,* **94,** 105–117, doi:10.1175/1520-0493(1966)094<0105:DAOTCD>2.3.CO;2.

McIntyre, M. E., and T. N. Palmer, 1983: Breaking planetary waves in the stratosphere. *Nature,* **305,** 593–600, doi:10.1038/305593a0.

Mo, K. C., and R. Higgins, 1998a: Tropical influences on California precipitation. *J. Climate,* **11,** 412–430, doi:10.1175/1520-0442(1998)011<0412:TIOCP>2.0.CO;2.

——, and R. W. Higgins, 1998b: Tropical convection and precipitation regimes in the western United States. *J. Climate,* **11,** 2404–2423, doi:10.1175/1520-0442(1998)011<2404:TCAPRI>2.0.CO;2.

Neiman, P. J., F. M. Ralph, G. A. Wick, Y.-H. Kuo, T.-K. Wee, Z. Ma, G. H. Taylor, and M. D. Dettinger, 2008a: Diagnosis of an intense atmospheric river impacting the Pacific Northwest: Storm summary and offshore vertical structure observed with COSMIC satellite retrievals. *Mon. Wea. Rev.,* **136,** 4398–4420, doi:10.1175/2008MWR2550.1.

——, ——, ——, J. D. Lundquist, and M. D. Dettinger, 2008b: Meteorological characteristics and overland precipitation impacts of atmospheric rivers affecting the west coast of North America based on eight years of SSM/I satellite observations. *J. Hydrometeor.,* **9,** 22–47, doi:10.1175/2007JHM855.1.

Newell, R. E., N. E. Newell, Y. Zhu, and C. Scott, 1992: Tropospheric rivers?—A pilot study. *Geophys. Res. Lett.,* **19,** 2401–2404, doi:10.1029/92GL02916.

Newman, M., G. N. Kiladis, K. M. Weickmann, F. M. Ralph, and P. D. Sardeshmukh, 2012: Relative contributions of synoptic and low-frequency eddies to time-mean atmospheric moisture transport, including the role of atmospheric rivers. *J. Climate,* **25,** 7341–7361, doi:10.1175/JCLI-D-11-00665.1.

Ralph, F. M., P. J. Neiman, and G. A. Wick, 2004: Satellite and CALJET aircraft observations of atmospheric rivers over the eastern North Pacific Ocean during the winter of 1997/98. *Mon. Wea. Rev.,* **132,** 1721–1745, doi:10.1175/1520-0493(2004)132<1721:SACAOO>2.0.CO;2.

——, ——, and R. Rotunno, 2005: Dropsonde observations in low-level jets over the northeastern Pacific Ocean from CALJET-1998 and PACJET-2001: Mean vertical-profile and atmospheric-river characteristics. *Mon. Wea. Rev.,* **133,** 889–910, doi:10.1175/MWR2896.1.

——, ——, G. A. Wick, S. I. Gutman, M. D. Dettinger, D. R. Cayan, and A. B. White, 2006: Flooding on California's Russian River: Role of atmospheric rivers. *Geophys. Res. Lett.,* **33,** L13801, doi:10.1029/2006GL026689.

——, ——, G. N. Kiladis, K. Weickmann, and D. W. Reynolds, 2011: A multiscale observational case study of a Pacific atmospheric river exhibiting tropical–extratropical connections and a mesoscale frontal wave. *Mon. Wea. Rev.,* **139,** 1169–1189, doi:10.1175/2010MWR3596.1.

——, and Coauthors, 2014: A vision for future observations for Western U.S. extreme precipitation and flooding. *J. Contemp. Water Res. Educ.,* **153,** 16–32, doi:10.1111/j.1936-704X.2014.03176.x.

Rienecker, M. M., and Coauthors, 2011: MERRA—NASA's Modern-Era Retrospective Analysis for Research and Applications. *J. Climate,* **24,** 3624–3648, doi:10.1175/JCLI-D-11-00015.1.

Rivière, G., 2010: Role of Rossby wave breaking in the west Pacific teleconnection. *Geophys. Res. Lett.,* **37,** L11802, doi:10.1029/2010GL043309.

Ropelewski, C., and M. S. Halpert, 1987: Global and regional scale precipitation patterns associated with the El Niño/Southern Oscillation. *Mon. Wea. Rev.,* **115,** 1606–1626, doi:10.1175/1520-0493(1987)115<1606:GARSPP>2.0.CO;2.

Ryoo, J., Y. Kaspi, D. Waugh, G. Kiladis, D. Waliser, E. Fetzer, and J. Kim, 2013: Impact of Rossby wave breaking on U.S. West Coast winter precipitation during ENSO events. *J. Climate,* **26,** 6360–6382, doi:10.1175/JCLI-D-12-00297.1.

Smith, B., S. Yuter, P. Neiman, and D. Kingsmill, 2010: Water vapor fluxes and orographic precipitation over northern California associated with a landfalling atmospheric river. *Mon. Wea. Rev.,* **138,** 74–100, doi:10.1175/2009MWR2939.1.

Sodemann, H., and A. Stohl, 2013: Moisture origin and meridional transport in atmospheric rivers and their association with multiple cyclones. *Mon. Wea. Rev.,* **141,** 2850–2868, doi:10.1175/MWR-D-12-00256.1.

Strong, C., and G. Magnusdottir, 2008a: How Rossby wave breaking over the Pacific forces the North Atlantic Oscillation. *Geophys. Res. Lett.,* **35,** L10706, doi:10.1029/2008GL033578.

——, and ——, 2008b: Tropospheric Rossby wave breaking and the NAO/NAM. *J. Atmos. Sci.,* **65,** 2861–2876, doi:10.1175/2008JAS2632.1.

Wheeler, M. C., and H. H. Hendon, 2004: An all-season real-time multivariate MJO index: Development of an index for monitoring and prediction. *Mon. Wea. Rev.,* **132,** 1917–1932, doi:10.1175/1520-0493(2004)132<1917:AARMMI>2.0.CO;2.

Wick, G. A., P. J. Neiman, and F. M. Ralph, 2013a: Description and validation of an automated objective technique for identification and characterization of the integrated water vapor signature of atmospheric rivers. *IEEE Trans. Geosci. Remote Sens.,* **51,** 2166–2176, doi:10.1109/TGRS.2012.2211024.

——, ——, ——, and T. M. Hamill, 2013b: Evaluation of forecasts of the water vapor signature of atmospheric rivers in operational numerical weather prediction models. *Wea. Forecasting,* **28,** 1337–1352, doi:10.1175/WAF-D-13-00025.1.

Wolter, K., and M. S. Timlin, 1998: Measuring the strength of ENSO events: How does 1997/98 rank? *Weather,* **53,** 315–324, doi:10.1002/j.1477-8696.1998.tb06408.x.

Zhu, Y., and R. E. Newell, 1998: A proposed algorithm for moisture fluxes from atmospheric rivers. *Mon. Wea. Rev.,* **126,** 725–735, doi:10.1175/1520-0493(1998)126<0725:APAFMF>2.0.CO;2.